Comparison Between Brain and Cerebellar Autoradiography Using [^{18}F]Flortaucipir, [^{18}F]MK6240, and [^{18}F]PI2620 in Postmortem Human Brain Tissue

Antonio Aliaga*[1–3], Joseph Therriault*[1,4,5], Kely Monica Quispialaya[1,3,5,6], Arturo Aliaga[1,5], Robert Hopewell[5], Nesrine Rahmouni[1,4,5], Arthur C. Macedo[1,4,5], Peter Kunach[1,4,5], Jean-Paul Soucy[5], Gassan Massarweh[5], Aida Abreu Diaz[7], Tharick A. Pascoal[8], Andreia Rocha[2], Marie-Christine Guiot[5], Luiza S. Machado[2], Marco Antônio De Bastiani[2], Débora Guerini de Souza[2], Diogo O. Souza[2], Serge Gauthier[1,4], Eduardo R. Zimmer[1,2,9], and Pedro Rosa-Neto[1,3,4,5]

[1]*Translational Neuroimaging Laboratory, McGill University Research Centre for Studies in Aging, Douglas Hospital, McGill University, Montreal, Quebec, Canada;* [2]*Graduate Program in Biological Sciences: Biochemistry, Universidade Federal do Rio Grande do Sul, Porto Alegre, Brazil;* [3]*Research Institute of McGill University Health Centre, Montreal, Quebec, Canada;* [4]*Department of Neurology and Neurosurgery, McGill University, Montreal, Quebec, Canada;* [5]*Montreal Neurological Institute, Montreal, Quebec, Canada;* [6]*Department of Medicine, McGill University, Montreal, Quebec, Canada;* [7]*Department of Pharmacology and Physiology, University of Montreal, Montreal, Quebec, Canada;* [8]*Department of Psychiatry, Pittsburgh University, Pittsburgh, Pennsylvania; and* [9]*Department of Pharmacology, Universidade Federal do Rio Grande do Sul, Porto Alegre, Brazil*

Our objective was to evaluate the in vitro binding properties of [^{18}F]flortaucipir, 6-(fluoro-^{18}F)-3-(1*H*-pyrrolo[2,3-c]pyridin-1-yl)isoquinolin-5-amine ([^{18}F]MK6240), and 2-(2-([^{18}F]fluoro)pyridin-4-yl)-9*H*-pyrrolo[2,3-b:4,5c′]dipyridine ([^{18}F]PI2620) head-to-head in postmortem human brain tissue. **Methods:** Autoradiography was used to assess uptake of [^{18}F]flortaucipir, [^{18}F]MK6240, and [^{18}F]PI2620 in control and Alzheimer disease (AD) autopsy-confirmed brain tissues. The study focused on the analysis of the prefrontal cortex, hippocampus, and cerebellum sections in 12 controls and 12 AD cases, as well as whole-brain hemisphere in 1 control and 1 AD sample, for each radiotracer. The binding values of [^{18}F]flortaucipir, [^{18}F]MK6240, and [^{18}F]PI2620 were calculated from regions of interest manually drawn in the prefrontal, hippocampal, and cerebellar cortices. **Results:** For all 3 radioligands investigated, we observed significant tracer binding differences between control and AD tissues in the whole-brain hemisphere, prefrontal cortex, and hippocampus but not in the cerebellar cortex. [^{18}F]MK6240 and [^{18}F]PI2620 had higher effect sizes to differentiate control and AD cases than did [^{18}F]flortaucipir. Bland–Altman analyses revealed strong correlations between [^{18}F]MK6240, [^{18}F]PI2620, and [^{18}F]flortaucipir, with the highest agreement found for [^{18}F]MK6240 versus [^{18}F]PI2620. **Conclusion:** The 3 radioligands showed comparable diagnostic properties to assess tau aggregates in vitro. Binding to AD brain tissues was higher for [^{18}F]MK6240 and [^{18}F]PI2620 than for [^{18}F]flortaucipir. Additionally, [^{18}F]MK6240 and [^{18}F]PI2620 had greater selectivity, displaying decreased uptake in control brain tissue compared with [^{18}F]flortaucipir. These results might provide insights on ongoing initiatives to create a universal scale for tau imaging studies.

Key Words: Alzheimer disease; [^{18}F]flortaucipir; [^{18}F]AV1451; [^{18}F]MK6240; [^{18}F]PI2620; autoradiography

J Nucl Med 2025; 66:123–129
DOI: 10.2967/jnumed.124.267539

Received Jan. 30, 2024; revision accepted May 13, 2024.
For correspondence or reprints, contact Pedro Rosa-Neto (pedro.rosa@mcgill.ca) or Eduardo R. Zimmer (eduardo.zimmer@ufrgs.br).
*Contributed equally to this work.
Published online Oct. 30, 2024.

In Alzheimer disease (AD), the progressive accumulation of tubulin-associated unit (tau) pathology in the form of neurofibrillary tangles is closely associated with cognitive status (*1–4*). Early tangle aggregation in medial temporal brain regions is associated with mild memory impairment (*3,5,6*), with widespread tangle aggregation over the neocortex strongly linked with dementia severity (*3,4,7*). In vivo quantification of tau pathology using PET allows the detection of early AD pathologic changes and shows promise in the differential diagnosis of dementia (*8,9*). Several tau PET imaging agents have been developed for in vivo quantification of tau tangle burden, including [^{18}F]flortaucipir, approved by the Food and Drug Administration, as well as second-generation imaging agents such as 6-(fluoro-^{18}F)-3-(1*H*-pyrrolo[2,3-c]pyridin-1-yl)isoquinolin-5-amine ([^{18}F]MK6240) and 2-(2-([^{18}F]fluoro)pyridin-4-yl)-9*H*-pyrrolo[2,3-b:4,5c′]dipyridine ([^{18}F]PI2620). Recent data suggest that second-generation tracers have both higher sensitivity and higher specificity for tau tangle aggregates, as well as higher selectivity for tau over monoamine oxidase (MAO) proteins, than does the first generation (*10–15*).

Autoradiography is a valuable technique to study protein binding sites in tissues, based on the distribution of specific molecular imaging agents (*16*). Autoradiographic evaluations of [^{18}F]flortaucipir (also referred to as [^{18}F]AV1451), [^{18}F]MK6240, and [^{18}F]PI2620 have demonstrated high specificity for the 3R + 4R tau characteristic of the neurofibrillary tangles observed in AD (*13,17–19*). However, previous autoradiography studies of tau PET imaging agents used ethanol washing protocols (*17–19*), which can remove the tracer from off-target binding sites such as MAO-A and MAO-B proteins (*20,21*). Nonspecific binding to MAO enzymes has been reported to influence [^{18}F]flortaucipir signal (*22,23*), possibly affecting the comparison between diagnostic groups. Autoradiography washing protocols without ethanol prevent tracer removal from off-target binding sites, offering a good approach to evaluate new ligands for in vivo PET imaging of tau pathology (*20,21,24*).

Autoradiographic data comparing the most common tracers used in clinical trials for AD might provide valuable insights on

ongoing attempts to create a universal scale for tau load, valid for all tau imaging agents (*25*). We predict a higher degree of association across high-tau regions and lower associations in brain regions with negligible tau burden. Comparisons of the binding properties of tau PET ligands using autoradiography are needed to clarify how analogous these tracers are in postmortem tissue. Here, we evaluate the binding properties of [^{18}F]flortaucipir, [^{18}F]MK6240, and [^{18}F]PI2620 head-to-head in postmortem human brain tissue.

MATERIALS AND METHODS

Radiosynthesis of [^{18}F]Flortaucipir, [^{18}F]MK6240, and [^{18}F]PI2620

[^{18}F]fluoride was produced via ^{18}O(p,n)^{18}F reaction in an IBA 18/9 Cyclone cyclotron and then transferred to an automated synthesis module. [^{18}F]MK6240 was synthesized according to a methodology previously described by our group (*26*). [^{18}F]PI2620 and [^{18}F]flortaucipir were synthesized similarly to previously published methodologies (*27,28*).

Tissue Samples

Frozen brain tissues were obtained from the Douglas-Bell Canada Brain Bank at the Douglas Mental Health University Institute. The postmortem tissues were classified as AD-positive or healthy control by the Consortium to Establish a Registry for Alzheimer Disease. The tissue collection and analysis were approved by the Brain Bank's and Douglas Institute's research ethics boards. The experiments were performed on a total of 39 control and 39 AD samples. The study comprised the analysis of the prefrontal cortex, hippocampus, and cerebellum sections in 12 controls and 12 AD tissues, as well as the whole-brain hemisphere in 1 control and 1 AD sample, for each radiotracer.

Tissue Preparation

Flash-frozen tissue blocks were received and placed inside the rotary cryostat (Leica CM3050) until thawed at −20°C. Subsequently, the fixed tissues were prepared for embedding within a supportive medium with paraffin. These tissues were then sliced into 20-μm-thick sections, mounted onto microscope slides on thawing, and stored at −80°C.

Autoradiography Imaging

On the experiment day, the frozen samples were thawed and allowed to air-dry at room temperature for 60 min. Subsequently, they were preincubated in a buffer solution (30 mM sodium 2-[4-(2-hydroxyethyl)piperazin-1-yl]ethane-1-sulfonate, 110 mM NaCl, 5 mM KCl, 2.5 mM $CaCl_2$, and 1.2 mM $MgCl_2$) with a pH of 7.4 for 30 min. Before autoradiography imaging, each radiotracer was mixed for 10 min with the buffer. The tissues were left to air-dry and then were incubated for 150 min with 22.31 MBq of [^{18}F]flortaucipir (0.0053 μg, 1,117.92 GBq/μmol), 20.17 MBq of [^{18}F]MK6240 (0.0118 μg, 476.52 GBq/μmol), or 22.13 MBq of [^{18}F]PI2620 (0.0038 μg, 1,537.65 GBq/μmol) in 650 mL of buffer solution each. After incubation, the sections were washed in ice-cold buffer (3 × 5 min), dipped in ice-cold distilled water (4 × 30 s), and dried under a stream of cool air for 20 min. Finally, the samples were transferred to phosphor imaging plates (Fuji film) for a 20-min exposure. The plates were imaged using an Amersham Typhoon biomolecular imager (spatial resolution, 50 μm).

Autoradiography Calibration

The experiments were designed to optimize the use of absolute quantification with autoradiography imaging. A calibration curve was prepared using [^{18}F]MK6240 standards with 8 radioactivity concentrations from 0.007 to 1.687 kBq/mg of solution. To calibrate the phosphor screen, 10-μL samples were placed on a thin-layer chromatography plate (Analtech) for exposure and imaging. The phantom circles were analyzed with the Fiji/ImageJ software (version V1.53v). A region of interest (ROI) was manually drawn on each spot, and the average gray value per square pixel was measured (Supplemental Fig. 1A; supplemental materials are available at http://jnm.snmjournals.org). In the Fiji/ImageJ software, the images were calibrated using the Rodbard (NIH Image) function. This provided the following standard calibration equation: $y = c \times [(x - a)/(d - x)]^{(1/b)}$, where y is the radioactivity concentration in the tissue (kBq/mg), x is the mean intensity of the pixel (0–255), $a = 51.605$, $b = 0.992$, $c = 18.554$, and $d = 299.963$. These parameters were then used to calculate the tracer binding in each image.

Quantitative Image Analysis

After autoradiography calibration, quantitative values of radioactivity concentration in tissues (kBq/mg) were obtained using the Fiji/ImageJ software with 2-dimensional ROIs manually drawn in the whole-brain hemispheres (15 ROIs each in the gray matter and in the background or nontarget area outside the tissues), prefrontal cortex, hippocampus, cerebellum, and background or nontarget areas. The activity concentration was measured in 5 equidistant ROIs placed in the gray matter of the prefrontal cortex, 1 ROI in the hippocampus, 5 ROIs each in the gray matter and in white matter of the cerebellum, and 5 ROIs in the background. The total binding was calculated as the average activity concentration in each brain region minus the corresponding average background activity concentration (Supplemental Figs. 1B and 1C).

Statistical Analysis

The tissue radioactivity concentrations in control and AD groups were compared using a 2-tailed t test with Welch correction using GraphPad Prism 10. A P value of 0.05 or less was considered statistically significant. Bland–Altman analyses assessed the agreement between measurements of [^{18}F]flortaucipir, [^{18}F]MK6240, and [^{18}F]PI2620.

RESULTS

A summary of the demographic characteristics of the individuals whose brain samples were studied is presented in Table 1. The mean age of the participants was 74.3 y (SD, 10.78 y), and 10 (41.6%) were women. The control and AD groups did not differ in age ($t(21) = 0.185$, $P = 0.855$), sex distribution ($t(22) = 1.685$, $P = 0.106$), or postmortem delay for tissue processing ($t(21) = 0.221$, $P = 0.827$). However, there was a significant difference in brain weight (13.44% lower in AD group than in control group, $t(19) = 2.84$, $P = 0.011$).

Autoradiography experiments revealed binding of [^{18}F]flortaucipir, [^{18}F]MK6240, and [^{18}F]PI2620 in control and AD brain slices, with higher radioactivity concentrations in AD tissues for all 3 radioligands (Fig. 1). Autoradiographic evaluation of these tracers in the prefrontal cortex, hippocampus, and cerebellum of control ($n = 12$/radiotracer) and AD ($n = 12$/radiotracer) brains are displayed in Figure 1A. Whole-brain hemispheres are presented in Figure 1B. Significant differences were observed between control and AD groups with [^{18}F]flortaucipir, [^{18}F]MK6240, and [^{18}F]PI2620 (Supplemental Fig. 2).

Head-to-Head Comparison of [^{18}F]Flortaucipir, [^{18}F]MK6240, and [^{18}F]PI2620 Binding in Prefrontal Cortex, Hippocampus, and Cerebellum

We observed significant differences between control and AD groups in the prefrontal cortex for [^{18}F]flortaucipir ($t = 4.26$, $P = 0.001$), [^{18}F]MK6240 ($t = 6.38$, $P < 0.0001$), and [^{18}F]PI2620 ($t = 6.37$, $P < 0.0001$) (Fig. 2A). Significant differences were

TABLE 1
Demographic Characteristics of Heathy Control and AD Brain Tissues

Pathologic diagnosis	Sex	Age at death (y)	Postmortem delay (h)	Brain weight (g)
Control	F	48	43.75	NA
Control	F	78	19.75	NA
Control	F	77	17.25	1,150
Control	F	82	32.50	NA
Control	M	76	20.50	1,320
Control	M	60	7.25	1,350
Control	F	74	11	1,365
Control	M	71	76	1,250
Control	F	90	13.37	1,050
Control	F	81	29	1,275
Control	M	91	6.75	1,070
Control	M	69	12	1,225
AD	M	63	15	1,165
Severe AD	F	77	9.25	905
Severe AD	M	76	8.5	1,240
Severe AD	F	84	11.75	980
AD	F	55	15.25	715
AD	M	67	96	1,010
Severe AD	M	92	13.25	1,200
AD	M	66	8.5	1,075
Severe AD	M	79	12.75	1,135
AD	M	79	24.75	1,210
Severe AD	M	76	24	1,005
AD	M	73	26.25	1,120

NA = not available.

also detected between control and AD groups in the hippocampus for [^{18}F]flortaucipir ($t = 3.95$, $P = 0.0009$), [^{18}F]MK6240 ($t = 5.92$, $P < 0.0001$), and [^{18}F]PI2620 ($t = 6.69$, $P < 0.0001$) (Fig. 2B). However, we found no difference between AD and control tissues when assessed by [^{18}F]flortaucipir ($t = 0.09$, $P = 0.93$), [^{18}F]MK6240 ($t = 0.93$, $P = 0.36$), and [^{18}F]PI2620 ($t = 0.70$, $P = 0.49$) in the cerebellar gray matter (Fig. 2C). When comparing the prefrontal cortex–to–cerebellar gray matter ratios, we observed significant differences for [^{18}F]flortaucipir ($t = 4.38$, $P = 0.0006$), [^{18}F]MK6240 ($t = 6.23$, $P < 0.0001$), and [^{18}F]PI2620 ($t = 6.51$, $P < 0.0001$). The comparison of hippocampus–to–cerebellar gray matter ratios also revealed significant differences for [^{18}F]flortaucipir ($t = 4.03$, $P = 0.0011$), [^{18}F]MK6240 ($t = 5.22$, $P = 0.0002$), and [^{18}F]PI2620 ($t = 6.48$, $P < 0.0001$) (Figs. 2D and 2E).

Correlation Between [^{18}F]Flortaucipir and [^{18}F]MK6240. A high agreement between [^{18}F]flortaucipir and [^{18}F]MK6240 was confirmed in the prefrontal cortex ($R = 0.934$, $P < 0.0001$), hippocampus ($R = 0.833$, $P < 0.0001$), and cerebellum ($R = 0.777$, $P < 0.0001$) (Fig. 3). When conducting a subgroup analysis in AD tissues only, we also found a strong correlation between [^{18}F]flortaucipir and [^{18}F]MK6240 in the prefrontal cortex ($R = 0.915$, $P < 0.0001$), hippocampus ($R = 0.737$, $P = 0.006$), and cerebellum ($R = 0.818$, $P = 0.001$). Bland–Altman analyses revealed substantial agreement between the radioligands, with lowest agreement in the cerebellar tissues (Fig. 3, bottom).

Correlation Between [^{18}F]Flortaucipir and [^{18}F]PI2620. [^{18}F]flortaucipir and [^{18}F]PI2620 results were highly correlated in the prefrontal cortex ($R = 0.922$, $P < 0.0001$) and hippocampus ($R = 0.792$, $P < 0.0001$) but not in the cerebellum ($R = 0.271$, $P = 0.201$) (Fig. 4). By performing a subgroup analysis in AD tissues only, we also found a strong correlation between these radioligands in the prefrontal cortex ($R = 0.920$, $P < 0.0001$) and hippocampus ($R = 0.620$, $P = 0.032$) but not in the cerebellum ($R = 0.149$, $P = 0.643$). Bland–Altman analyses revealed substantial agreement between radioligands, which again was lower in the cerebellar tissues (Fig. 4, bottom).

Correlation Between [^{18}F]MK6240 and [^{18}F]PI2620. We found strong correlations between [^{18}F]MK6240 and [^{18}F]PI2620 in the prefrontal cortex ($R = 0.987$, $P < 0.0001$) and hippocampus ($R = 0.957$, $P < 0.0001$) but not in the cerebellum ($R = 0.352$, $P = 0.092$) (Fig. 5). When conducting a subgroup analysis in AD tissues only, we detected strong correlations between [^{18}F]MK6240 and [^{18}F]PI2620 in the prefrontal cortex ($R = 0.980$, $P < 0.0001$) and hippocampus ($R = 0.927$, $P < 0.0001$) but not in the cerebellum ($R = 0.393$, $P = 0.206$). Bland–Altman analyses

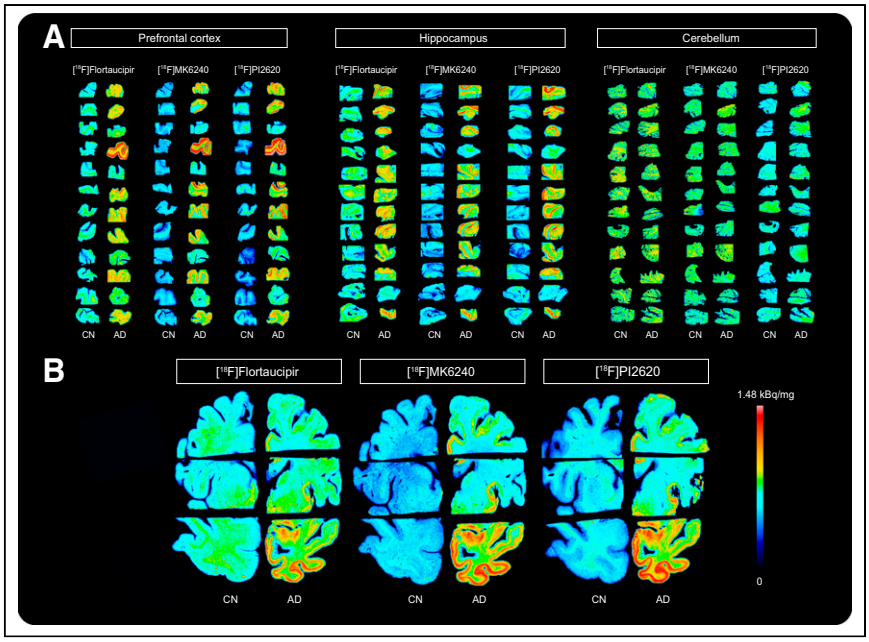

FIGURE 1. Autoradiography images showing binding of [^{18}F]flortaucipir, [^{18}F]MK6240, and [^{18}F]PI2620 in prefrontal cortex, hippocampus, and cerebellum (A) and in whole-brain hemisphere (B) of control and AD brains. CN = control.

revealed substantial agreement between radioligands (the highest agreement between pairs of radioligands), which was also lower in the cerebellar tissues (Fig. 5, bottom).

Gray Matter of Prefrontal Cortex, Hippocampus, and Cerebellum in Control Tissues

Significant differences between prefrontal gray matter and hippocampal gray matter were detected with [^{18}F]flortaucipir and [^{18}F]PI2620. In contrast, there was no difference between these regions with [^{18}F]MK6240. Furthermore, we observed significant differences between prefrontal gray matter and cerebellar gray matter with [^{18}F]MK6240 and [^{18}F]PI2620 but no differences with [^{18}F]flortaucipir. Finally, we found significant differences between hippocampal gray matter and cerebellar gray matter tissues with [^{18}F]flortaucipir, [^{18}F]MK6240, and [^{18}F]PI2620. The comparison between prefrontal cortex gray matter–to–cerebellar gray matter and hippocampal gray matter–to–cerebellar gray matter ratios revealed significant differences for [^{18}F]flortaucipir and [^{18}F]PI2620 but not for [^{18}F]MK6240 (Supplemental Fig. 3).

Gray Matter and White Matter in Cerebellum

Statistical analysis indicated no differences between cerebellar gray matter and white matter control tissues with [^{18}F]flortaucipir and [^{18}F]MK6240. In contrast, we found significant differences with [^{18}F]PI2620 in the control and AD tissues when comparing tracer binding in the gray matter and white matter of the cerebellum (Supplemental Fig. 4).

DISCUSSION

This study directly compared the binding properties of [^{18}F]flortaucipir, [^{18}F]MK6240, and [^{18}F]PI2620 in the same postmortem sections of human brain tissue. We report that binding in AD tissues was significantly higher for [^{18}F]MK6240 and [^{18}F]PI2620 than for [^{18}F]flortaucipir. Additionally, binding in control brain tissue was lower for [^{18}F]MK6240 and [^{18}F]PI2620 than for [^{18}F]flortaucipir. Taken together, these results suggest that second-generation tau ligands are better at discriminating controls versus late-stage AD in vitro, supporting their use in vivo as PET imaging agents.

Tau PET is increasingly used as a secondary outcome measure in disease-modifying clinical trials (*29–31*). Because AD is a neurodegenerative disease that progresses over the course of decades (*32–34*), only small annual changes are expected to be detectable using PET. Therefore, imaging agents with high affinity and specificity for their target are preferred for detecting signals of disease progression and modification. Our study provides evidence that [^{18}F]flortaucipir, [^{18}F]MK6240, and [^{18}F]PI2620 are highly sensitive imaging agents for the quantification of tau pathology in AD but that [^{18}F]MK6240 and [^{18}F]PI2620 have sensitivity superior to that of [^{18}F]flortaucipir for the presence of tau tangles. These results agree with studies showing that [^{18}F]MK6240 and [^{18}F]PI2620 have 3- to 5-fold higher affinities for tau

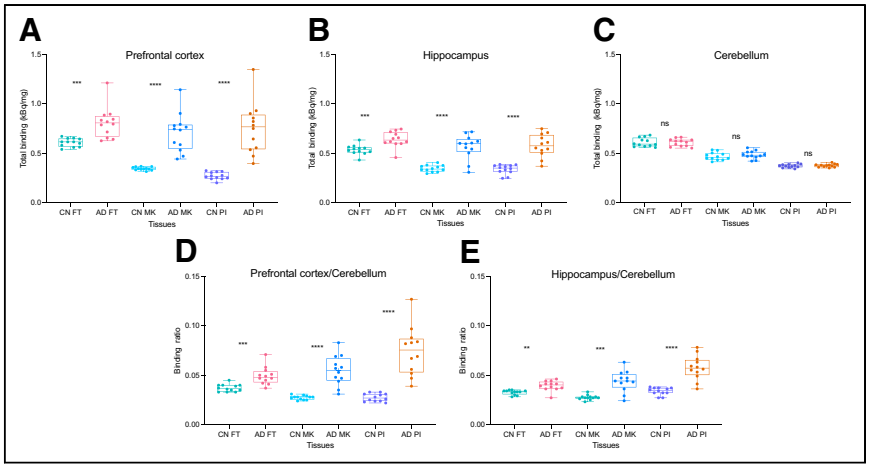

FIGURE 2. (A–C) Total binding of [^{18}F]flortaucipir, [^{18}F]MK6240, and [^{18}F]PI2620 in prefrontal cortex (A), hippocampus (B), and cerebellum gray matter (C). (D and E) Prefrontal cortex–to–cerebellum (D) and hippocampus-to-cerebellum (E) ratios. Significant differences between control and AD tissues were present for binding of [^{18}F]flortaucipir (n = 12), [^{18}F]MK6240 (n = 12), and [^{18}F]PI2620 (n = 12) in prefrontal cortex and hippocampus, but no significant differences were found in cerebellar gray matter. Significant differences between control and AD tissue ratios (prefrontal cortex to cerebellum gray matter, hippocampus to cerebellum gray matter) were present for [^{18}F]flortaucipir, [^{18}F]MK6240, and [^{18}F]PI2620. $^{**}P < 0.01$. $^{***}P < 0.001$. $^{****}P < 0.0001$. CN = control; FT = [^{18}F]flortaucipir; MK = [^{18}F]MK6240; ns = not significant; PI = [^{18}F]PI2620.

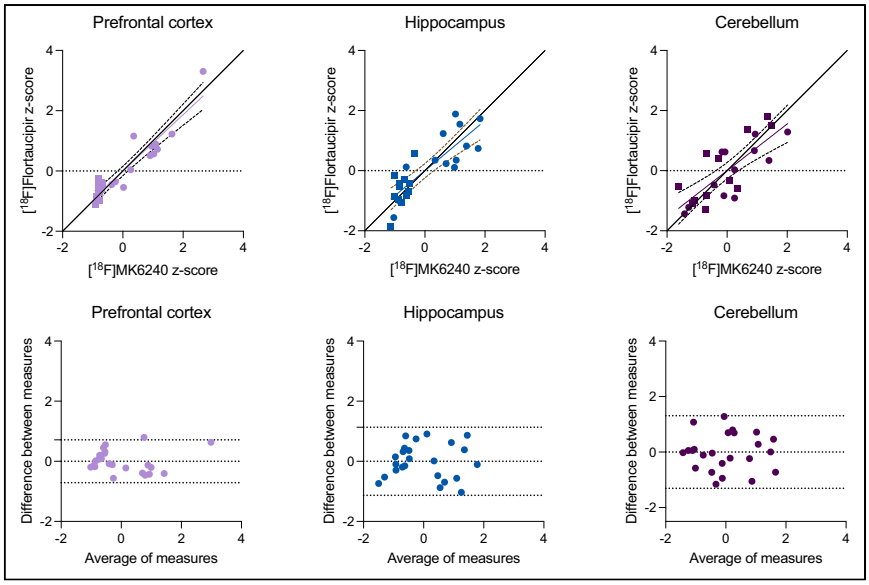

FIGURE 3. Relationship between [^{18}F]flortaucipir and [^{18}F]MK6240 binding. (Top) Linear relationship between [^{18}F]flortaucipir and [^{18}F]MK6240 in prefrontal cortex, hippocampus, and cerebellar gray matter. Circles and squares indicate measurements of AD and control tissues, respectively. For prefrontal cortex and hippocampus, linear relationship close to line of origin was observed. (Bottom) Bland–Altman analysis assessing bias between [^{18}F]flortaucipir and [^{18}F]MK6240 uptake. Dashed lines indicate limits of agreement. Cerebellum had largest difference between measurements.

tangles than does [^{18}F]flortaucipir (*10,12,13*). In fact, recent cryogenic electron microscopy studies support distinct relationships between tau imaging agents and tau fibrils described in this study (*35,36*).

The selectivity of tau imaging agents also influences their interpretation (*37*). In our study, we observed that [^{18}F]flortaucipir had higher levels of binding in control brains. Specifically, in individuals without AD, there was nearly a 200% difference in tissue concentration between [^{18}F]flortaucipir and [^{18}F]MK6240 or [^{18}F]PI2620 in the prefrontal cortex and a 150% difference in the hippocampus. The higher levels of binding in control brains result in a lower effect size for differentiating between controls and individuals with AD. Consequently, this issue complicates establishing thresholds of tau PET abnormality for [^{18}F]flortaucipir and reduces the usefulness of [^{18}F]flortaucipir as an outcome measure in clinical trials seeking to detect subtle changes in tau PET. The source of the off-target binding of [^{18}F]flortaucipir has often been speculated to be MAO-A. Some in vitro studies have provided evidence of MAO-A binding (*22,23,38*), though the magnitude to which this off-target binding confounds in vivo [^{18}F]flortaucipir PET data is controversial (*20,22*). It is also possible that off-target binding of [^{18}F]flortaucipir concerns several nonspecific targets and is region-dependent (*39*). Interestingly, a recent autoradiographic study conducted by Aguero et al. revealed strong binding of [^{18}F]flortaucipir, [^{18}F]MK6240, and [^{18}F]PI2620 in cortical regions containing tau tangles from AD brains, but no binding signal was detected for any of the 3 radioligands in control cases (*19*). The use of ethanol in autoradiography washing protocols has been reported to induce removal of weaker tracer off-target binding (*20,21*), often associated with MAO proteins (*20*). However, the qualitative comparison performed by Aguero et al. yielded identical results for the 3 radioligands even when avoiding methanol or ethanol in fixation or washing steps. Similar off-target profiles were found for these tracers exhibiting nonspecific binding to neuromelanin, melanin, and brain hemorrhagic lesions and weak or no binding to MAO-A and MAO-B enzymes (*19*). Autoradiography methodologies may differ among studies on several factors (e.g., slice thickness; brain region; disease stage; tracer concentration and molar activity; and fixing, preincubation, incubation, washing, drying, and imaging protocols), which might contribute to inconsistent results. The discrepancies from different studies on [^{18}F]flortaucipir off-target binding underscore the importance of a deeper comparison of autoradiography protocols, along with a larger number of inhibitors, brain regions, and Braak tangle stages, to allow for a better comprehension of tau ligand binding properties for in vivo PET imaging.

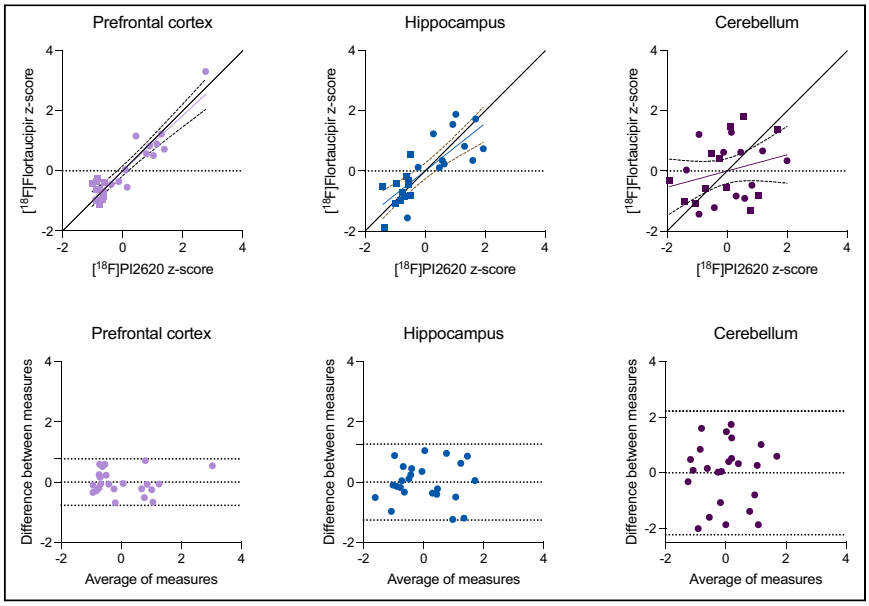

FIGURE 4. Relationship between [^{18}F]flortaucipir and [^{18}F]PI2620 binding. (Top) Linear relationship between [^{18}F]flortaucipir and [^{18}F]PI2620 in prefrontal cortex, hippocampus, and cerebellar gray matter. Circles and squares indicate measurements of AD and control tissues, respectively. For prefrontal cortex and hippocampus, linear relationship close to line of origin was observed. (Bottom) Bland–Altman analysis assessing bias between [^{18}F]flortaucipir and [^{18}F]PI2620 uptake. Dashed lines indicate limits of agreement. Cerebellum had largest difference between measurements.

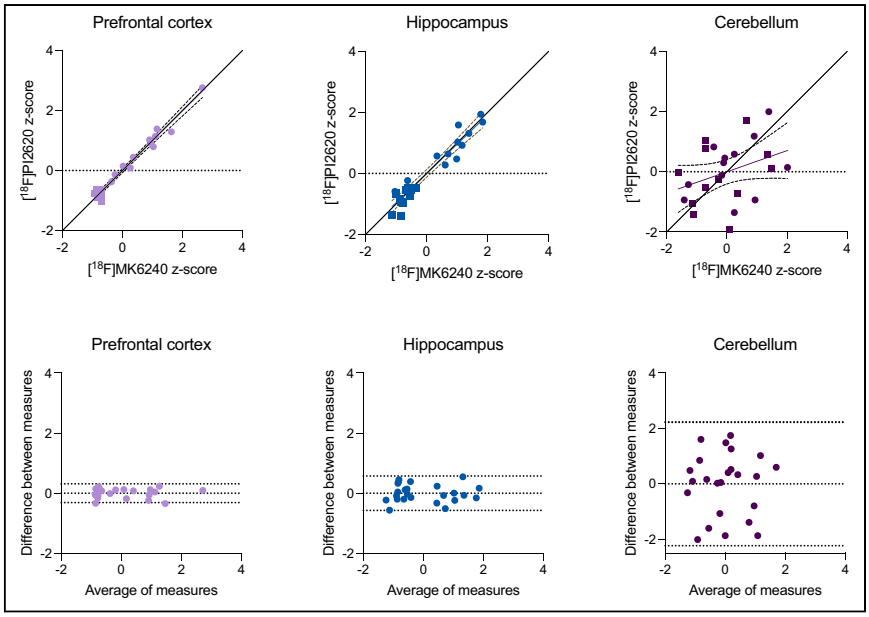

FIGURE 5. Relationship between [^{18}F]MK6240 and [^{18}F]PI2620 binding. (Top) Linear relationship between [^{18}F]MK6240 and [^{18}F]PI2620 in prefrontal cortex, hippocampus, and cerebellar gray matter. Circles and squares indicate measurements of AD and control tissues, respectively. For prefrontal cortex and hippocampus, linear relationship close to line of origin was observed. (Bottom) Bland–Altman analysis assessing bias between [^{18}F]MK6240 and [^{18}F]PI2620 uptake. Dashed lines indicate limits of agreement. Cerebellum had largest difference between measurements.

The present study provides a quantitative head-to-head comparison of [^{18}F]flortaucipir, [^{18}F]MK6240, and [^{18}F]PI2620 in tau tangle and cerebellar regions in AD brains compared with control tissues in a large number of samples. Our findings agree with clinical PET studies showing off-target binding of [^{18}F]flortaucipir versus high selectivity for tau tangle regions of the second-generation radioligands [^{18}F]MK6240 and [^{18}F]PI2620 (*15,22,23,38*).

Finally, when discussing selectivity, it is important to mention that ^{3}H- or ^{18}F-labeled PI2620 has exhibited specific binding to tau aggregates in non-AD tauopathies, though typically at lower affinity than to AD-type tau (*11,13,21,40*). In addition, Varlow and Vasdev (*21*) demonstrated that ethanol washing decreases the background signal and washes away a portion of [^{3}H]PI2620-specific binding in chronic traumatic encephalopathy brain tissues. This also points out the impact of autoradiography methodology on some controversial results of tau PET tracers binding in non-AD tissues (*11,13,19,21,40*).

In direct head-to-head comparisons, we observed strong relationships between concentrations of [^{18}F]flortaucipir, [^{18}F]MK6240, and [^{18}F]PI2620 in postmortem human brain tissue. The strong relationships between [^{18}F]MK6240 and [^{18}F]PI2620 are in line with a recent competition binding study showing that these radioligands have similar binding sites (*11*). Although we observed higher effect sizes of [^{18}F]MK6240 and [^{18}F]PI2620 to differentiate between AD and control brains, Bland–Altman analyses revealed strong correlations between all z-scored tau PET imaging agents. It is remarkable that for all 3 tau PET tracers, the largest SDs between measurements were observed in the cerebellum, suggesting that these tracers may have particular nonspecific binding profiles, as tau tangle pathology is not observed in the cerebellum (*1,2*). Interestingly, higher [^{18}F]flortaucipir uptake in the cerebellum might contribute to its lower dynamic range. Furthermore, using the cerebellum as a reference region for [^{18}F]flortaucipir may contribute to its smaller effect sizes when differentiating between AD and non-AD groups. The larger variance observed in the cerebellum might not have significant implications for cross-sectional diagnostic studies, which typically report high performance of [^{18}F]flortaucipir (*8*); however, this larger variance could be a confounding factor for longitudinal studies and clinical trials attempting to measure subtle tau PET changes.

Our study also showed that in control individuals, the prefrontal cortex, hippocampus, and cerebellum uptake relationships were different for the 3 radioligands, suggesting the regional differences in nonspecific binding. Further studies are needed to assess the impact of these observations when considering the cerebellum as a reference region. Additionally, the comparison between gray and white matter uptake values in control and AD tissues demonstrated different behaviors of the radioligands. This finding suggests that using white matter as a reference region (*41*) may be less suitable for detecting longitudinal tau PET change, since other factors such as white matter off-target binding and generation of radiometabolites might play a role.

Although autoradiography might present insights on the interpretation of in vivo imaging, it is important to acknowledge certain limitations. First, the binding properties described in this study, measured with autoradiography, do not perfectly recapitulate in vivo tau PET binding properties. For example, in vivo PET signals using simplified semiquantitative methods can be influenced by tracer delivery and washout (*42*). Second, the restricted number of sampled brain regions also represents a limitation. Furthermore, it is unknown to what extent tau PET imaging agents can detect very small amounts of tau tangles in early Braak regions. Because the present study assessed brain tissue samples of individuals with advanced or severe AD, future studies should evaluate tau PET autoradiography in milder AD cases. Finally, our findings relate to total tissue uptake rather than specific binding.

CONCLUSION

The 3 radioligands showed comparable diagnostic properties to assess tau aggregates in vitro. [^{18}F]MK6240 and [^{18}F]PI2620 exhibited higher binding to AD brain tissues than did [^{18}F]flortaucipir. Additionally, [^{18}F]MK6240 and [^{18}F]PI2620 had greater selectivity for tau tangles, displaying decreased uptake in control brain tissue compared with [^{18}F]flortaucipir. The excellent in vitro binding properties of [^{18}F]MK6240 and [^{18}F]PI2620 support their use in vivo as PET imaging agents for AD diagnosis.

DISCLOSURE

Study funding was provided by the Colin J. Adair Charitable Foundation, McGill University Faculty of Medicine, Alzheimer's Society of Canada, Alzheimer's Association, Fonds de Recherche du Québec, Weston Brain Institute, and Canadian Institutes of Health Research. Joseph Therriault has received consultancy fees

from the Neurotorium educational platform, outside the scope of the present work. Pedro Rosa-Neto has served on scientific advisory boards or as a consultant for Roche, Novo Nordisk, Eisai, and Cerveau Technologies. Eduardo Zimmer has served on the scientific advisory board of Nintx, Novo Nordisk, and Masima. He is also a cofounder and a minority shareholder at Masima. No other potential conflict of interest relevant to this article was reported.

KEY POINTS

QUESTION: Do [^{18}F]flortaucipir, [^{18}F]MK6240, and [^{18}F]PI2620 have similar in vitro binding properties in postmortem human brain tissue?

PERTINENT FINDINGS: The uptake of [^{18}F]flortaucipir, [^{18}F]MK6240, and [^{18}F]PI2620 was evaluated by autoradiography in control and AD brain tissues. The 3 ligands showed comparable diagnostic properties to assess tau aggregates in vitro, with significant differences between control and AD in whole brain, prefrontal cortex, and hippocampus. [^{18}F]MK6240 and [^{18}F]PI2620 exhibited higher binding to AD brain tissues and greater selectivity than [^{18}F]flortaucipir.

IMPLICATIONS FOR PATIENT CARE: Our findings might provide insights on ongoing initiatives to create a universal scale for tau imaging studies.

REFERENCES

1. Braak H, Braak E. Staging of Alzheimer's disease-related neurofibrillary changes. *Neurobiol Aging.* 1995;16:271–278.
2. Braak H, Braak E. Neuropathological stageing of Alzheimer-related changes. *Acta Neuropathol (Berl).* 1991;82:239–259.
3. Therriault J, Pascoal TA, Lussier FZ, et al. Biomarker modeling of Alzheimer's disease using PET-based Braak staging. *Nat Aging.* 2022;2:526–535.
4. Jagust W. Imaging the evolution and pathophysiology of Alzheimer disease. *Nat Rev Neurosci.* 2018;19:687–700.
5. Crary JF, Trojanowski JQ, Schneider JA, et al. Primary age-related tauopathy (PART): a common pathology associated with human aging. *Acta Neuropathol (Berl).* 2014;128:755–766.
6. Johnson KA, Schultz A, Betensky RA, et al. Tau positron emission tomographic imaging in aging and early Alzheimer disease. *Ann Neurol.* 2016;79:110–119.
7. Pascoal TA, Therriault J, Benedet AL, et al. ^{18}F-MK-6240 PET for early and late detection of neurofibrillary tangles. *Brain.* 2020;143:2818–2830.
8. Ossenkoppele R, Rabinovici GD, Smith R, et al. Discriminative accuracy of [^{18}F]flortaucipir positron emission tomography for Alzheimer disease vs other neurodegenerative disorders. *JAMA.* 2018;320:1151–1162.
9. Macedo AC, Tissot C, Therriault J, et al. The use of tau PET to stage Alzheimer disease according to the Braak staging framework. *J Nucl Med.* 2023;64:1171–1178.
10. Malarte ML, Nordberg A, Lemoine L. Characterization of MK6240, a tau PET tracer, in autopsy brain tissue from Alzheimer's disease cases. *Eur J Nucl Med Mol Imaging.* 2021;48:1093–1102.
11. Malarte ML, Gillberg PG, Kumar A, Bogdanovic N, Lemoine L, Nordberg A. Discriminative binding of tau PET tracers PI2620, MK6240 and RO948 in Alzheimer's disease, corticobasal degeneration and progressive supranuclear palsy brains. *Mol Psychiatry.* 2023;28:1272–1283.
12. Hostetler ED, Walji AM, Zeng Z, et al. Preclinical characterization of ^{18}F-MK-6240, a promising PET tracer for in vivo quantification of human neurofibrillary tangles. *J Nucl Med.* 2016;57:1599–1606.
13. Kroth H, Oden F, Molette J, et al. PI-2620 lead optimization highlights the importance of off-target assays to develop a PET tracer for the detection of pathological aggregated tau in Alzheimer's disease and other tauopathies. *J Med Chem.* 2021; 64:12808–12830.
14. Ng KP, Therriault J, Kang MS, et al. Rasagiline, a monoamine oxidase B inhibitor, reduces in vivo [^{18}F]THK5351 uptake in progressive supranuclear palsy. *Neuroimage Clin.* 2019;24:102091.
15. Leuzy A, Chiotis K, Lemoine L, et al. Tau PET imaging in neurodegenerative tauopathies: still a challenge. *Mol Psychiatry.* 2019;24:1112–1134.
16. Caro LG, Van Tubergen RP, Kolb JA. High-resolution autoradiography. *J Cell Biol.* 1962;15:173–188.
17. Lowe VJ, Curran G, Fang P, et al. An autoradiographic evaluation of AV-1451 tau PET in dementia. *Acta Neuropathol Commun.* 2016;4:58.
18. Aguero C, Dhaynaut M, Normandin MD, et al. Autoradiography validation of novel tau PET tracer [F-18]-MK-6240 on human postmortem brain tissue. *Acta Neuropathol Commun.* 2019;7:37.
19. Aguero C, Dhaynaut M, Amaral AC, et al. Head-to-head comparison of [^{18}F]-flortaucipir, [^{18}F]-MK-6240 and [^{18}F]-PI-2620 postmortem binding across the spectrum of neurodegenerative diseases. *Acta Neuropathol (Berl).* 2024;147:25.
20. Wright JP, Goodman JR, Lin Y-G, et al. Monoamine oxidase binding not expected to significantly affect [^{18}F]flortaucipir PET interpretation. *Eur J Nucl Med Mol Imaging.* 2022;49:3797–3808.
21. Varlow C, Vasdev N. Evaluation of tau radiotracers in chronic traumatic encephalopathy. *J Nucl Med.* 2023;64:460–465.
22. Vermeiren C, Motte P, Viot D, et al. The tau positron-emission tomography tracer AV-1451 binds with similar affinities to tau fibrils and monoamine oxidases. *Mov Disord.* 2018;33:273–281.
23. Lemoine L, Leuzy A, Chiotis K, Rodriguez-Vieitez E, Nordberg A. Tau positron emission tomography imaging in tauopathies: the added hurdle of off-target binding. *Alzheimers Dement (Amst).* 2018;10:232–236.
24. Parent MJ, Bedard M-A, Aliaga A, et al. Cholinergic depletion in Alzheimer's disease shown by [^{18}F]FEOBV autoradiography. *Int J Mol Imaging.* 2013;2013:205045.
25. Villemagne VL, Leuzy A, Bohorquez SS, et al. CenTauR: toward a universal scale and masks for standardizing tau imaging studies. *Alzheimers Dement (Amst).* 2023; 15:e12454.
26. Hopewell R, Ross K, Kostikov A, et al. A simplified radiosynthesis of [^{18}F]MK-6240 for tau PET imaging. *J Labelled Comp Radiopharm.* 2019;62:109–114.
27. Kroth H, Oden F, Molette J, et al. Discovery and preclinical characterization of [^{18}F]PI-2620, a next-generation tau PET tracer for the assessment of tau pathology in Alzheimer's disease and other tauopathies. *Eur J Nucl Med Mol Imaging.* 2019; 46:2178–2189.
28. Chien DT, Bahri S, Szardenings AK, et al. Early clinical PET imaging results with the novel PHF-tau radioligand [F-18]-T807. *J Alzheimers Dis.* 2013;34:457–468.
29. Rafii MS, Sperling RA, Donohue MC, et al. The AHEAD 3-45 study: design of a prevention trial for Alzheimer's disease. *Alzheimers Dement.* 2023;19:1227–1233.
30. van Dyck CH, Swanson CJ, Aisen P, et al. Lecanemab in early Alzheimer's disease. *N Engl J Med.* 2023;388:9–21.
31. Mintun MA, Lo AC, Duggan Evans C, et al. Donanemab in early Alzheimer's disease. *N Engl J Med.* 2021;384:1691–1704.
32. Villemagne VL, Burnham S, Bourgeat P, et al. Amyloid-β deposition, neurodegeneration, and cognitive decline in sporadic Alzheimer's disease: a prospective cohort study. *Lancet Neurol.* 2013;12:357–367.
33. Jack CR, Knopman DS, Jagust WJ, et al. Tracking pathophysiological processes in Alzheimer's disease: an updated hypothetical model of dynamic biomarkers. *Lancet Neurol.* 2013;12:207–216.
34. Bateman RJ, Xiong C, Benzinger TLS, et al. Clinical and biomarker changes in dominantly inherited Alzheimer's disease. *N Engl J Med.* 2012;367:795–804.
35. Kunach P, Vaquer-Alicea J, Smith MS, et al. Cryo-EM structure of Alzheimer's disease tau filaments with PET ligand MK-6240. bioRxiv website. https://www.biorxiv.org/content/10.1101/2023.09.22.558671v1. Published September 22, 2023. Accessed June 3, 2024.
36. Shi Y, Murzin AG, Falcon B, et al. Cryo-EM structures of tau filaments from Alzheimer's disease with PET ligand APN-1607. *Acta Neuropathol (Berl).* 2021;141: 697–708.
37. Klunk WE. Molecular imaging: what is right and what is an illusion? *Alzheimers Dement (Amst).* 2018;10:217–220.
38. Drake LR, Pham JM, Desmond TJ, et al. Identification of AV-1451 as a weak, nonselective inhibitor of monoamine oxidase. *ACS Chem Neurosci.* 2019;10:3839–3846.
39. Baker SL, Harrison TM, Maass A, La Joie R, Jagust WJ. Effect of off-target binding on ^{18}F-flortaucipir variability in healthy controls across the life span. *J Nucl Med.* 2019;60:1444–1451.
40. Varlow C, Mathis CA, Vasdev N. In vitro evaluation of [^{3}H]PI-2620 and structural derivatives in non-Alzheimer's tauopathies. *Nucl Med Biol.* 2024;130-131:108891.
41. Young CB, Landau SM, Harrison TM, Poston KL, Mormino EC. Influence of common reference regions on regional tau patterns in cross-sectional and longitudinal [^{18}F]-AV-1451 PET data. *Neuroimage.* 2021;243:118553.
42. Lammertsma AA. Quantification of PET studies. *J Nucl Cardiol.* 2019;26: 2045–2047.